

Exotic high pressure behavior of light alkali metals, lithium and sodium

B. Rousseau^{1,2}, Y. Xie³, Y. Ma³, and A. Bergara^{1,2,4,a}

¹ Donostia International Physics Center (DIPC), Paseo de Manuel Lardizabal 4, 20018, Donostia, Basque Country, Spain

² Centro de Física de Materiales (CFM) CSIC-UPV/EHU, 1072 Posta kutxatila, 20080 Donostia, Basque Country, Spain

³ State Key Lab of Superhard Materials, Jilin University, Changchun 130012, P.R. China

⁴ Materia Kondentsatuaren Fisika Saila, Zientzia eta Teknologia Fakultatea, Euskal Herriko Unibertsitatea, 644 Postakutxatila, 48080 Bilbo, Basque Country, Spain

Received 10 December 2010

Published online 13 April 2011 – © EDP Sciences, Società Italiana di Fisica, Springer-Verlag 2011

Abstract. At ambient conditions, lithium and sodium behave as free-electron metals and adopt highly symmetric close-packed structures. Under high pressure, however, these simple metals undergo a series of complex phase transitions to structures of lower symmetry, along with significant changes of their physical properties. In this review we provide a comprehensive description of these light alkali metals, with a focus on the structural and electronic properties under pressure.

1 Introduction

Lithium, element 3 in the periodic table, and sodium, element 11, are often quoted as textbook examples of simplicity [1]. Indeed, at ambient conditions, these monovalent elements adopt the simple body-centered cubic structure (bcc), leaving a single valence electron per primitive unit cell. Their transport properties are consistent with nearly spherical Fermi surfaces (in fact measured to be so with exquisite accuracy in the case of Na) and the valence electrons appear to be nearly free.

Based on their apparent simplicity at room conditions, the standard view of the alkalis used to be that their simplicity should be re-enforced by pressure. Indeed, it is expected that at sufficiently small ionic volume Ω , the kinetic energy of the electrons (which scales as $1/\Omega^{2/3}$) should dominate their potential energy (which, for a perfect Coulomb interaction, would scale as $1/\Omega^{1/3}$) and that the ultimate faith of any pressurized system is to become a free electron-like metal, with the ions adopting a close-packed configuration. At first sight, it appears that the alkali metals have reached this high pressure limit already at ambient conditions, and pressure should only make them *more* free electron-like.

This intuitive picture is in fact quite wrong for pressures currently attainable experimentally, up to hundreds of gigapascals (GPa). Although the ultimate faith of the alkalis is to become simple and free electron-like at ultra-high pressures, this limit is far from achieved at ambient conditions as these systems exhibit pressure-induced structural complexity.

2 Lithium

The simple view that lithium should remain simple under pressure was challenged by the theoretical prediction that under compression it would yield lower-coordinated structures starting at $\simeq 45$ GPa, with the orthorhombic $Cmca$ structure being favored above $\simeq 100$ GPa (about four fold compression) [2,3]. This latter structure can be obtained continuously from the fcc arrangement to yield a configuration in which lithium ions are clearly seen to form pairs; the associated band structure is semimetallic, almost that of a zero-gap semi-conductor. It was also reported, counter intuitively, that the valence band width narrowed under pressure and that the band gaps at the zone faces became very large compared to the band width, indicating a *strong* electron-ion effective interaction, quite at odds with the original assumption that the alkalis are nearly free electron metals [1,4]. Although not unheralded (similar band width narrowing had been reported before in lithium [2,3,5], but only for the fcc structure, and at a pressure that would prove well beyond the stability range of that phase), these calculations offered deep insights into the origin of the breakdown of nearly free electron behavior. Indeed, it was argued that the combined effects of the Pauli exclusion principle and orthogonality render the ionic cores repulsive to valence states; as the volume of the sample decreases under pressure, the relative volume of the rather incompressible cores increases, forcing the valence density to localize into interstitial regions. As will be discussed below, this turns out to be a common factor in the various phases of lithium at high pressure, and can in fact be taken as a better paradigm than the nearly free electron approximation [4,6].

^a e-mail: a.bergara@ehu.es

Lithium is challenging to study experimentally at high pressures. Firstly, it only has three electrons and thus its X-ray scattering is rather weak. The use of intense synchrotron radiation is thus a must to obtain useful X-ray diffraction data. Secondly, lithium is highly reactive, and can interact with the diamond anvil cell (DAC) [7,8]. Furthermore, lithium can leak out through the very tight space between the gasket and the diamond anvil.

2.1 Crystal phases

Lithium, like all the alkalis, crystallizes in the bcc structure at ambient conditions and transforms to the fcc structure under moderate compression (about 7.5 GPa in the case of lithium [9]). This apparent simplicity disappears at lower temperatures as lithium undergoes a martensitic transformation near 70 K. The low temperature phase was initially thought to be hcp, was later resolved to the so-called samarium 9R structure [10] (an arrangement of hexagonal layers with the sequence ABCBCACAB), but it was more recently suggested that in fact the low temperature crystalline arrangement of lithium is a disordered polytype exhibiting short-range ordering of hcp, fcc and 9R type [11]. Computations treating the ionic dynamics at the level of the volume dependent quasiharmonic approximation were sufficient to show that the stabilization of bcc with temperature is entropically driven [12]. Incidentally, this vexing low temperature complexity results in the Fermi surface of lithium, the so-called simple metal *par excellence*, to be unknown experimentally even at low pressure because de Haas-van Alphen experiments cannot be conducted [1].

Stimulated by the provocative suggestions made by Neaton and Ashcroft [2], lithium was compressed at 180 K up to 50 GPa [7], leading to the discovery of two new crystalline phases. It was found that the fcc arrangement gives way to a structure with space group $R\bar{3}m$ at 39 GPa (Pearson symbol $hR1$; see Fig. 2) which in turn transforms to a novel phase at 42 GPa. This phase, which is shown in Fig. 1, has cubic symmetry and 16 ions in the unit cell (Pearson symbol $cI16$). It can be considered as consisting of a $2 \times 2 \times 2$ bcc supercell with a small displacement of the atoms along the cell's diagonal. First principles calculations confirmed that the $hR1$ and $cI16$ phases have lower enthalpy in their ranges of stability than the initially suggested $Cmca$ phase; however, the calculated electronic density showed pronounced maxima in the interstitial regions [7], in agreement with the general idea of Neaton and Ashcroft [2].

Up until very recently, experimental evidence for phase transitions beyond $cI16$ was scarce and incomplete. An X-ray diffraction experiment, conducted at 25 K and at pressures up to 86 GPa [13], presented evidence for two new phase transitions at 69 and 86 GPa. However, the diffraction patterns collected were not sufficient to resolve the crystalline structures of the proposed new phases. These phases, dubbed as Li-VI and Li-VII, were later found to be semiconducting [14] with resistivities several orders of magnitude larger than those in the metallic $cI16$

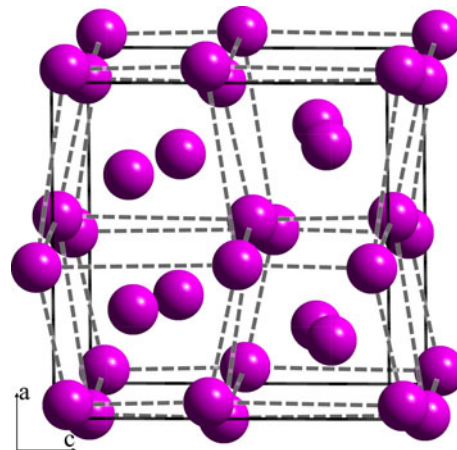


Fig. 1. The atomic arrangement for the $cI16$ structure viewed down the b axis. The dashed lines indicate the eight distorted bcc cells.

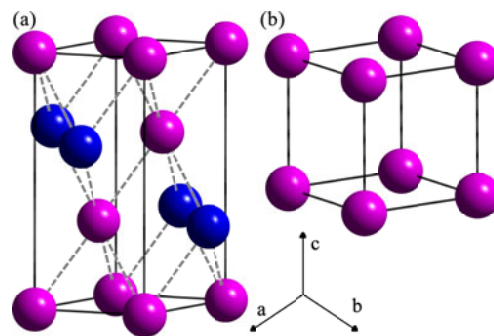


Fig. 2. The atomic arrangement in the unit cell of the $hR1$ structure viewed in (a) the hexagonal and (b) the rhombohedral coordinate system. The blue atoms in (a) are out of the unit cell.

phase. The formation of the Li-VI and Li-VII phases was also observed by other means. Indeed, a transition was suggested to occur at about 66 GPa based on the observed change in the superconducting transition temperature [15], which correlates well with the more recent X-ray experiment [13]. Also, Raman spectra collected on samples of ${}^6\text{Li}$ and ${}^7\text{Li}$ up to 123 GPa at about 180 K suggest the presence of two unknown phases, one between 55 and 69 GPa, and the other above [16], again in agreement with X-ray diffraction [13]. Very interestingly, a high frequency Raman band with frequency $\simeq 1800 \text{ cm}^{-1}$ was identified in this Li-VII phase with an isotope coefficient,

$$\alpha \equiv -\text{Log} \left[\frac{\omega({}^6\text{Li})}{\omega({}^7\text{Li})} \right] / \left[\frac{M({}^6\text{Li})}{M({}^7\text{Li})} \right], \quad (1)$$

which strongly departed from the ideal BCS value of $1/2$. This was interpreted as evidence that the high pressure phase arranges the ions in pairs interacting with a strongly anharmonic potential. Phonons were computed for various competing structures and none could attain the large frequency observed in the experiment, reaching at most frequencies in the 1200 cm^{-1} range [17] (it should be

noted however that these computations were performed in the harmonic approximation). Very recently, the phase diagram of lithium was mapped out experimentally over an unprecedented range of pressures (up to 130 GPa), as well as a wide range of temperatures (from 77 K to 300 K) [18]. The experimental problems inherent to compressing lithium were circumvented by using synchrotron radiation, the smallest possible sample chamber and low temperatures. The experiment clearly identified three new phases beyond *cI16*, all orthorhombic C-face centered. Proceeding at 200 K, it was found that *cI16* yields to a phase with 88 lithium ions per unit cell (and thus dubbed *oC88*) at 60 GPa. This latter phase only has a narrow stability range and was found to transform to *oC40* at 70 GPa and 150 K. These last two phases were visually observed to be grey and dark respectively, in agreement with previous resistivity measurements indicating the presence of a Li-VI and a Li-VII phase in this pressure range [14]. Finally, upon further compression, the *oC40* phase was found to transform to *oC24* beyond about 100 GPa. Although the cell dimensions and number of ions per cell could be deduced for the novel high pressure phases, difficulties in acquiring high-quality data prevented the determination of the ionic positions for the *oC88*, *oC40* and *oC24* phases.

Many candidate structures for lithium beyond 50 GPa have been suggested based on ab initio simulations before the phase diagram was resolved experimentally. A new phase with 24 ions per unit cell, named *Cmca-24*, was proposed by allowing a supercell arrangement of the structure proposed by Neaton and Ashcroft (henceforth *Cmca-16*) to equilibrate using constant volume molecular dynamics simulated annealing [19]. This phase was found to have lower enthalpy than the *Cmca-16* phase and didn't show the "strikingly short" Li-Li distances exhibited by this latter structure. It was also calculated to have a lower enthalpy than the experimentally confirmed *cI16* phase above 88 GPa. It is also noteworthy that every ion in the *Cmca-24* structure has three nearest neighbors with which it adopts a trigonal planar geometry. Notably, the ions in the *cI16* structure also have three nearest neighbors, but form a trigonal pyramidal configuration, which flattens under pressure to eventually come to resemble the *Cmca-24* local arrangement. In this sense, *Cmca-24* appears to be a natural continuation of the *cI16* phase, whereas *Cmca-16* is not [19]. The *Cmca-24* phase was also observed to display large interstitial density accumulation, which was attributed to a change from σ to π bonding as the lithium ions are brought together, a generic feature which should affect the local ionic arrangement irrespective of the exact structure. The stability of the *Cmca-24* phase was also confirmed by the use of a genetic algorithm applied to crystal structure prediction, as implemented in the USPEX program [20–22], by simulations based on the "ab initio random structure searching" (AIRSS) method [23–26], and with a newly developed particle swarm optimization technique for crystal structure prediction, as implemented in the CALYPSO program [27–29]. Finally, the data corresponding to the

measured high pressure structure named *oC24* [18] was further analysed and found to in fact correspond to the *Cmca-24* structure, with atomic coordinates in excellent agreement with values obtained from ab initio [30].

In light of the experimental fact that lithium becomes a semi-conductor in the Li-VI and Li-VII phases [14] (which were later identified as *oC88* and *oC40* [18]), two new insulating structures were proposed as having lowest enthalpy in that pressure range [31]. These structures, with symmetry *C2* and *Aba2* respectively (henceforth *C2-24* and *Aba2-24*, emphasising the number of ions in the cell), have small band gaps (on the order of 0.3 eV) in agreement with the observed semi-conducting behavior. On the other hand, these structures were found to only be very marginally favored, with an enthalpy difference with *Cmca-24* on the order of 1 meV, which is within the precision of ab initio total energy calculations; furthermore, these phases cannot explain the previously observed high frequency lithium vibrations [16]. Simulations based on particle swarm optimization (CALYPSO) [32] predicted that an orthorhombic structure with 40 ions per cell and symmetry *Aba2* (henceforth *Aba2-40*) has significantly lower enthalpy than *C2-24* and *Aba2-24* [30,32]; this phase was later confirmed to be the experimental *oC40* structure [18,30]. It is noteworthy however that harmonic phonon calculations yield maximum phonon frequencies of about 900 cm^{-1} [30], leaving the issue of the observed 1800 cm^{-1} vibron unresolved. The *oC88* phase was also studied [30]; simulations based on the AIRSS method and constrained by the experimental data of Guillaume et al. [18] found the most likely structure to have symmetry *C2mb*. Computations found this phase to have a *higher* enthalpy than the *cI16* phase in the range of pressures where the *oC88* phase is experimentally stable; the difference is small however, and it was suggested that dynamical effects could stabilize *C2mb* with respect to *cI16* [30].

Many structures have been predicted to be stable at higher pressures beyond the current experimental range. Many suggestions based on the AIRSS method were presented; although the *Cmca-24* phase was found to be most stable up to 247 GPa, many other similar structures with almost degenerate enthalpies were also found, suggesting that experiments might actually probe disordered mixtures of these phases [33]. A phase with space group symmetry *P4₁32* with sixfold coordinated ions was suggested to become preferred above about 300 GPa [34]. A new structure with *P4₂/mbc* symmetry with threefold coordination was later suggested to become more stable than *Cmca-24* above 247 GPa and to always be more stable than *P4₁32* [33]. This structure was found to yield to a new phase of *R $\bar{3}m$* symmetry at 449 GPa, which in turn transforms to the diamond structure at 483 GPa, calculated to be stable up to 1 TPa; these last two phases exhibit fourfold coordination, thus suggesting a transition from three to fourfold coordination under pressure, a feature echoed in simulations of the liquid phase of lithium [35], as will be discussed later. Very recently, the CALYPSO method predicted that a new threefold coordinated structure of symmetry *Cmca*

containing 56 ions per cell is more stable than $P4_2/mbc$ for pressure between 185 and 269 GPa [32].

Giant experimental advances have been made recently, mapping very accurately the phase diagram of lithium up to about 130 GPa. These new results, as well as numerous ab initio simulations, suggest a trend of *increasing* complexity with pressure, with the expected ultimate close-packed structures still nowhere in sight.

2.2 Liquid phase and melting curve

Measuring the melting curve of lithium is very difficult owing to its reactivity at high temperature and pressure. It has recently been measured up to 15 GPa, reproducing lower pressure results (see [36] and reference therein), and very recently lithium's phase diagram was mapped with great precision, including the general shape of the melting curve up to about 70 GPa [18]. Lithium melts at about 450 K at ambient pressure, and the melting curve is found to be “normal” (the melting temperature monotonically increasing with pressure) up to about 10 GPa where a melting curve maximum is observed at about 520 K. Interestingly, there was no indication of the bcc \rightarrow fcc transition observed at $\simeq 7.5$ GPa, suggesting that the pressure at which this transition occurs is shifted up at higher temperatures.

Preliminary calculations have been conducted based on the Lindemann criterion [37] which suggested that the melting curve should remain flat and not have a maximum. In view of the experimental results, it appears a more sophisticated theoretical approach is necessary to understand the melting of lithium.

First principles molecular dynamics (FPMD) simulations were conducted to understand the behavior of lithium in the liquid phase and to predict the melting curve [35]. By studying the pair correlation function $g(r)$ as well as the average angular arrangement between near neighbors at 1000 K, it was found that three distinct regions with different liquid structures could be identified. In the first region, for which $r_s \geq 2.6$ ($P \leq 23$ GPa), it was found that the liquid progresses from bcc-like to fcc-like local order. On the other hand, in the second region, for which $2.05 \leq r_s \leq 2.6$ ($23 \text{ GPa} \leq P \leq 150 \text{ GPa}$), the coordination *decreases* and the liquid acquires a $cI16$ -like local order. Finally, in the third region, for which $r_s \leq 2.05$ ($P \geq 150 \text{ GPa}$), the first coordination shell evolves to become composed of only four neighbors, with angular analysis revealing that they are tetrahedrally arranged about the reference ion. An estimate of the melting curve was also obtained using a “heat until it melts” approach: the melting curve was found to be rather flat above the bcc stability region and to increase rapidly to a maximum around 650 K near 20 GPa above the fcc stability region, after which the melting curve drops precipitously until it reaches an apparent minimum above the $cI16$ stability region.

The experiments of Lazicki et al. [36] and Guillaume et al. [18] confirm that there is a maximum in the melting curve, and the melting seems to follow the general trend

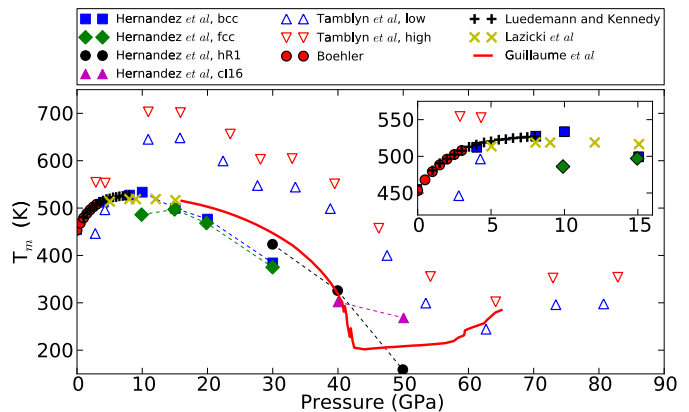


Fig. 3. Lithium experimental melting temperatures as measured by Boehler [38], Luedemann and Kennedy [39], Lazicki et al. [36] and Guillaume et al. [18], compared with calculated melting temperatures of Hernández et al. [40] and Tamblýn et al. [35]. The inset shows the low pressure region in greater detail.

described by Tamblýn et al. [35]. However, the position of this maximum and the subsequent anomalous melting curve is not well described quantitatively by these simulations. The melting curve of lithium was also studied recently using FPMD simulations with the “coexistence method”, where both solid and liquid phases are initially present [40] (see Fig. 3 for a comparison between different theoretical calculations and experimental data). In this method, one phase eventually vanishes from the simulation cell in favor of the stable phase if the thermodynamic variables do not correspond to the melting curve; the method then consists in finding (P, T) points where both phases survive for long simulation times, indicating a point on the melting line. This method avoids overheating (or supercooling) effects, which might explain the disagreement between experiments and previous simulations. It is also noteworthy that the simulations of Hernández et al. [40] contain an order of magnitude more simulated particles than the simulation of Tamblýn et al. [35], which helps minimize finite-size effects. The new simulations also reveal a maximum in the melting curve and a significant decrease of the melting temperature up to 50 GPa, the maximum pressure considered, and agree very well with all experimental data [18,36]. It is also found that the melting temperature of the bcc phase is always higher than that of the fcc phase up to 30 GPa, suggesting that lithium might transform from the fcc to the bcc with rising temperature and then melt from the bcc; this is consistent with the fact that experiments did not observe indication of bcc \rightarrow fcc phase transitions (i.e., lithium remained in the bcc phase near the melting temperature for pressures above the one at which low temperature bcc lithium is found to transform to the fcc structure).

It was recently confirmed that the melting temperature decreases dramatically with pressure from about 15 to 50 GPa, in agreement with predictions based on simulations. It remains a challenge to measure the local order in the liquid phase. If technical difficulties related

to lithium’s high reactivity can be resolved, it will be interesting to see if the local order in the liquid reflects the complexity of the crystalline phases, as simulations have suggested.

2.3 Electronic structure

Great insights into the behavior of lithium under pressure can be achieved through band structure calculations. These are typically done using density functional theory [41,42] as implemented in various computer programs. These simulations can lead to quantitatively very precise results, but they can also be invaluable tools to understand intuitively physical phenomena by providing information that is not readily accessible through experiment. The ability to compute the total energy (or enthalpy, or free energy, depending on the situation) allows band structure theorists to predict to some extent the structure lithium should adopt under pressure, but being able to separate this energy into well defined, coherent contributions leads to a much better grasp of the nature of the competition between phases, as is being able to compute the ground state electronic density corresponding to a given structure. This naturally leads to two complementary intuitive pictures of lithium under pressure.

The first of these pictures focuses on the energetic and reciprocal space view of the system. The stable structure of lithium under given thermodynamic conditions must minimize the appropriate free energy, which can be split into various contributions. The total energy is dominated by a “band structure” term, the energy associated with the occupied one-electron states of the Kohn-Sham problem, and a Madelung term, the electrostatic energy associated with the distribution of electronic and nuclear charge. At ambient pressure the ionic cores are relatively small, the electron gas is nearly free and the occupied band structure nearly oblivious to the specific ionic arrangement. The two dominant contributions to the energy are then practically decoupled and the ionic structure simply must minimize the Madelung energy, which it does by adopting a close-packed arrangement. Under pressure however the effective interactions between band electrons and ions become stronger, as reflected in large band gaps in the band structure at zone faces [2], and the band structure contribution to the total energy becomes quite sensitive to structure. Such a system is then susceptible to structural symmetry-breaking distortions, often referred to as either the Hume-Rothery [43], Peierls [2,19,35], Jahn-Teller [33] or “Fermi sphere Brillouin zone interaction” [44–46] mechanism (in this context, all these expressions have basically the same meaning). A favored distortion will modify the shape of the first Brillouin zone (1BZ) from that of the more symmetric ionic arrangement, bringing zone faces closer to the Fermi surface; this strongly perturbs the bands near the Fermi level. Occupied levels go down in energy whereas empty levels go up (as expected from perturbation theory and level repulsion) and the distortion can lead to a net gain in band structure energy. If this gain can overcome the Madelung energy cost of setting up

the distortion, then the lower symmetry phase is indeed more stable [45]. An important consequence of this is that the electronic density of states should be suppressed at the Fermi energy as the distortion drives states below it; this is a common feature observed in many calculations of the density of states of lithium in high pressure structures (predicted or experimental) [7,31,33,34,45].

A second, complementary picture that emerges from ab initio calculations is based on the real space distribution of electronic charge density. A common feature of the latter is that it tends to localize in the interstitial spaces of high pressure structures while being depressed between near neighbors [2,7,33–35]. This can be interpreted as the consequence of strongly repulsive ionic cores [2], or alternatively as a transition between s - σ bonding at low pressure, which tends to deposit electronic charge between near neighbors, to p - π bonding at high pressure, which deposit electronic charge *away* from the line of sight between neighbors. This was instructively illustrated for a linear chain of lithium ions as the inter-ionic distance was systematically reduced [19,47]. In turn, the favored structures are reminiscent of cation sublattices of binary compounds [7], suggesting that lithium becomes an electride where electronic piles of charge provide effective counterpart anions to the lithium cations [33].

These pictures are two sides of the same coin. As the relative volume occupied by the ionic cores increases, the electronic system can lower its kinetic energy by pushing the ions closer together (the Peierls distortion) to open up larger interstitial regions where to pile up electrons; in turn, these interstitial piles can advantageously be arranged like the anions of a binary compound. Moreover, these interstitial regions are poorly connected because of the trapping effect of the surrounding ions, explaining the shrinking band width.

2.4 Optical properties

The changes in the band structure induced by the increasing structural complexity under pressure has consequences on the response properties of the electronic sub-system. The computed Fermi surface, shown in Figure 4, is found to be rather spherical at ambient pressure, as expected from the nearly free electron model; however, under pressure in the fcc phase the Fermi surface is observed to develop copper-like necks at the L point of the 1BZ, as well as nesting [43] (see Fig. 5; see also [48] for a two dimensional analogue). Given that states become occupied at L, the long wavelength (i.e. $\mathbf{q} \rightarrow \mathbf{0}$) dynamic susceptibility is significantly modified and fcc lithium develops a novel, undamped plasmon at about $\hbar\omega \simeq 5$ –6 eV for pressures from 10 to 40 GPa [49,50]. This plasmon occurs independently of the usual, highly damped free electron-like plasmon and leads to a complete loss of reflectivity at 5 to 7 eV for pressures in the stability range of the fcc phase. The effect of pressure-induced increasing electronic localization on this plasmon has also been studied through the inclusion of so-called “local field effects” which account for the inhomogeneity of the electron gas [51]. In the fcc

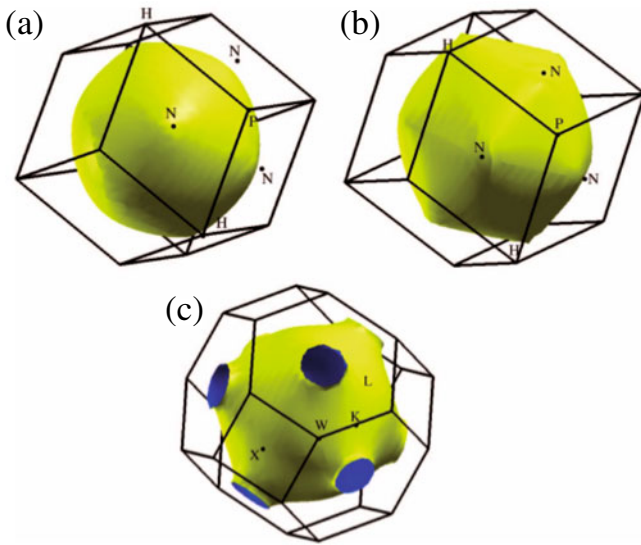


Fig. 4. Fermi surface of bcc lithium at (a) equilibrium and (b) $P = 8$ GPa and (c) fcc lithium at $P = 30$ GPa. At $P = 30$ GPa the Fermi surface develops increasing copper-like necks along ΓL and an extended nesting along several directions. Reprinted figure with permission from [43]. Copyright (2006) by the American Physical Society.

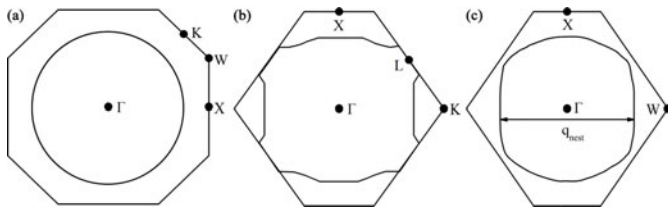


Fig. 5. Computed Fermi surface cross sections of fcc lithium at 30 GPa on the (a) $\Gamma K X$ (100), (b) $\Gamma K L$ (110) and (c) $\Gamma W X$ (111) planes. The $\Gamma K L$ and $\Gamma W X$ planes present a clear nesting in the ΓK and ΓW directions, respectively. Reprinted figure with permission from [43]. Copyright (2006) by the American Physical Society.

phase it is found that local field effects induce the periodic return of the plasmon peak for \mathbf{q} outside the 1BZ, and that its amplitude is very anisotropic.

Given that structural determination is difficult in high pressure phases of lithium, it has been suggested that optical properties might also be useful in distinguishing phases from one another. The interband contribution to the imaginary dielectric tensor was computed for the bcc, fcc, $hR1$ and $cI16$ phases at a volume corresponding to a pressure of about 40 GPa [52]. It was found that the imaginary dielectric tensor is very similar in the bcc, fcc and $hR1$ phases, but that it changes dramatically in the $cI16$ phase, which is attributed to the nearly parallel bands introduced near the Fermi energy by the symmetry lowering distortion leading to this phase.

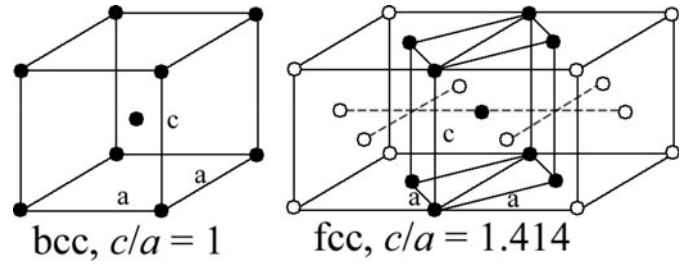


Fig. 6. The bcc and fcc structure represented assuming a bct structure. In the fcc case, a half of the bct structure is a quarter of the fcc structure.

2.5 Mechanisms of the high-pressure phase transitions

Often a phase transformation can be related to a particular normal mode of the system. Lowering of the frequency of this mode (the soft phonon mode) can indicate an upcoming phase transition. In such cases, the phonon frequency would go to zero, but more commonly the transition involves both the vibrational mode and an elastic modulus. Hence, the phonon softening and elastic instability are very critical for studying the mechanism of the phase transition.

Rodríguez-Prieto et al. [43] have studied the lattice dynamic properties of bcc lithium and found that the bcc to fcc phase transition is related to the softening of the transverse acoustic (TA) phonon mode along the $[0\xi\xi]$ -direction near the Brillouin zone center. The electronic, dynamical and elastic properties of the bcc alkali metals at high pressure have been extensively explored [53]. Analysis of the calculated results suggested that the instability of the C' tetragonal shear modulus associated with the TA phonon softening is driving the phase transition in the bcc alkali metals. A consequence of the C' instability is a transition from the bcc to a body-centered tetragonal (bct) structure. Notably, both the bcc and fcc structures can be described as bct structures (see Fig. 6). In the bcc structure, all three lattice vectors have equal length a , whereas in the fcc case a and b are equal and c has length $\sqrt{2}a$. Thus, the bcc-fcc transformation can be described by the tetragonal Bain's path [54], a continuous change of the c/a ratio from 1 to $\sqrt{2}$. Rodríguez-Prieto et al. [43,55] also suggested that Fermi surface nesting (FSN) combined with TA phonon softening along the Γ -K symmetry direction at 30 GPa could be the origin of the complex phase transitions beyond fcc in lithium.

2.6 Superconductivity and phonon instabilities

Superconductivity is certainly one of the most intriguing properties which a condensed matter system can exhibit, and for a long time it was thought that lithium just wasn't a good candidate for it [56,57].

Early estimates for the superconducting transition temperature (T_c) in lithium at ambient pressure based on the McMillan equation suggested a value around 1 K, even for the experimental 9R structure [58], in contrast

to the then known experimental upper limit of 6 mK. A more sophisticated approach treating electron-electron and electron-phonon interactions on the same footing (but neglecting to some extent the details of the band structure) suggested $T_c \simeq 0.4$ mK [59]. That estimate fell astonishingly close to the mark, as superconductivity was later observed in lithium at roughly that temperature [60].

The superconducting transition temperature, which is vanishingly small at ambient pressure, is found to increase by many orders of magnitude as pressure is applied. A first hint of this was observed as a sharp resistance drop in lithium at about 7 K under a pressure of 2 GPa [61]; this could not unequivocally be attributed to a transition to the superconducting state because no attempt was made at observing the Meissner effect. The onset of superconductivity in lithium under pressure was further explored in an other resistance-based experiment [62], where the sample was put in a pit bored directly in the face of one of the DAC's diamond to minimize leakage. Shimizu and colleagues could not measure the Meissner effect because of technical difficulties, but they still gave strong evidence that the transition was indeed to the superconducting state by observing the appropriate behavior as a function of an applied magnetic field. They found that T_c rises from zero at about 30 GPa and reaches a maximum of 20 K at 45 GPa. There is a fair bit of variance between sample runs in the experimental results, which has been attributed to the fact that no pressure medium was used, thus potentially causing anisotropic stress [63]. A subsequent experiment designed to observe the Meissner effect [15] confirmed the onset of superconductivity in the fcc phase above 20 GPa, reaching 16 K at the transition to the $hR1$ phase, dropping to about 10 K in that phase, and rising again to 16–18 K in the $cI16$ phase; lithium was found to still superconduct at 80 GPa, with $T_c \simeq 10$ K. A more recent experiment, conducted using helium as a pressure medium and thus resolving the issue of anisotropic stresses, revealed the non-monotonous behavior of T_c with pressure [64]. No superconducting transition was observed above 4 K below 20 GPa, or at 67 GPa, the highest pressure considered. Between these pressures, T_c rises to about 14 K at 30 GPa, abruptly changes slope and decreases from 30 to 50 GPa, and rises again before vanishing (within the resolution of the experiment). The analysis of the behavior of T_c with an applied magnetic field are consistent with type I superconductivity. A recent experiment probing superconductivity using the resistivity method confirmed qualitatively the findings of Deemyad and Schilling, and pushed further to find no transition above 8 K at 86 GPa [13,65].

These surprising experimental findings naturally stimulated theoretical work aimed at explaining the unusual behavior of T_c . An early calculation of T_c in the fcc and $cI16$ phases, based on the McMillan formula and the rigid muffin-tin approximation (RMTA), suggested that the superconducting transition temperature could be as large as 80 K [67]. This was clearly not observed, and was initially attributed to a failure of the RMTA [68]. However, T_c was calculated again using a similar method [69] and

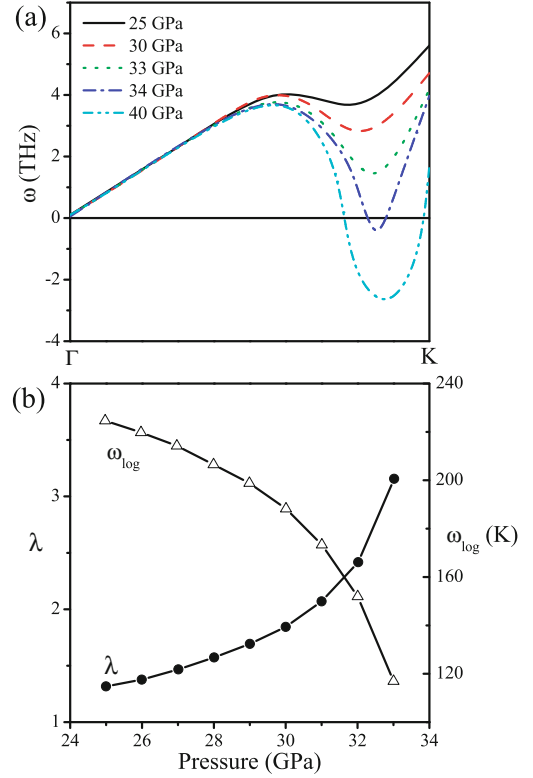


Fig. 7. (a) Evolution of the acoustic phonon branch for fcc Li along the Γ -K direction for pressures in the range 25–40 GPa, and (b) corresponding computed λ and ω_{\log} up to transition pressure to the $cI16$ phase. Image reproduced using data from reference [66].

the results are in excellent agreement with experiment in the fcc phase. Good agreement with experimental results in the fcc phase was also obtained by using both the recently developed “superconducting density functional theory” (SCDFT [70]) and the McMillan formula with a large value of μ^* [71]. It has been argued that the so-called Anderson morel parameter should be large in lithium ($\mu^* \simeq 0.2$ instead of the “usual” $\mu^* \simeq 0.1$) [59], a feature confirmed by the comparative McMillan-SCDFT study of Profeta et al. by noting that the density of electronic states is increased at the Fermi energy due to the proximity of a Van Hove singularity, brought on by the copper-like necks in the Fermi surface [43]. The rise of T_c under pressure in the fcc phase is then explained in terms of a transverse phonon softening along Γ -K-X, as shown in Figure 7, which in turn is due to Fermi surface nesting [43,71,72]. The softening phonons then yield an increasing contribution to the mass enhancement parameter λ , explaining the dramatic increase of T_c in the fcc phase. Given the excellent qualitative agreement between theory and experiment, Profeta and colleagues rule out the possibility of spin fluctuation playing an important role in lithium at these pressures: their calculations however fail to explain why the experimental T_c has a turnover while still in the fcc phase. It was shown that the bulk of the contribution to λ comes from narrow “hot spots” on

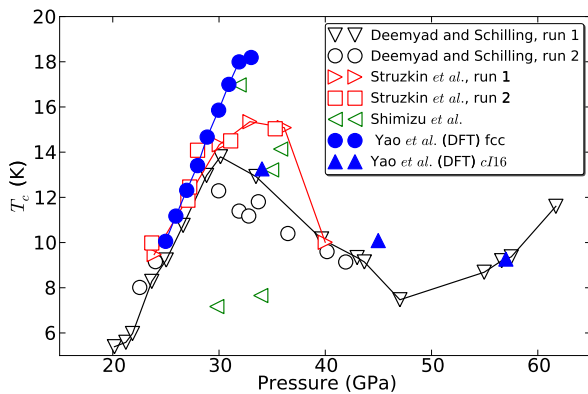


Fig. 8. Calculated values of T_c as a function of pressure (full symbols) for fcc and *cI16* Li of Yao et al. [66], compared to experimental results (open symbols) of Deemyad and Schilling [64], Shimizu et al. [62] and Struzkin et al. [15]. Full lines are simple guides for the eye.

the Fermi surface, showing that precise computations of λ could be quite taxing numerically [73].

Superconductivity in the *cI16* phase was studied by solving the isotropic Eliashberg equations for the superconducting gap [66]. Results, which can be seen in Figure 8, are in good agreement with experimental data points of Deemyad and Schilling [64], however using $\mu^* \simeq 0.12$, suggesting that electron-electron interactions are not so strong in *cI16* as in fcc. It was also found that nesting is much less important in *cI16* than in fcc, and that correspondingly there is a reduction in the phonon spectral weight at small frequencies, leading to smaller λ in the *cI16* phase.

What emerges from the various calculations performed so far is that lithium is a BCS-like phonon-mediated superconductor up to pressures where the *cI16* phase is stable. The dramatic increase of T_c in the fcc phase is due to phonon softening as the transition pressure is approached. Theoretical calculations overshoot T_c in the vicinity of the transition to *cI16*, which has been suggested as potentially caused by anharmonicity [66]. Although it appears that the effective Coulomb repulsion μ^* must be chosen to be large in the fcc phase, whereas it returns to a more “usual” value in the *cI16* phase, T_c appears to be well described by the McMillan equation. More sophisticated treatment of superconductivity would be laborious and would probably not yield further insight into the nature of superconductivity in lithium at pressures up to 70 GPa. No experimental data above that pressure are available. It would be interesting to see if as pressure is increased beyond the current limits, lithium adopts structures in which the valence electrons are more and more localized in interstitial regions and if that leads to strong correlation signatures in the superconducting state.

3 Sodium

Sodium, like lithium, has revealed itself to have a rich phase diagram under pressure. Although it shares some

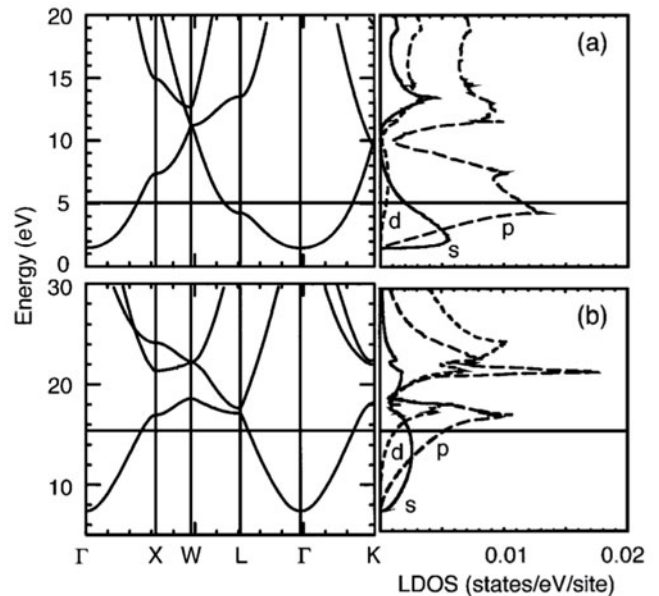


Fig. 9. Band structures, and *s*, *p* and *d* local densities of states at $r_s = 2.3$ for fcc (a) lithium ($P \simeq 60$ GPa) and (b) sodium ($P \simeq 245$ GPa). Solid horizontal lines denote the Fermi energies. The free electron values for the Fermi energy at this density is 9.47 eV. The *2s* and *2p* bandwidths in sodium at this density are 1.25 and 3.5 eV, respectively; the *1s* bands in lithium are 0.7 eV wide. Reprinted figure with permission from [74]. Copyright (2001) by the American Physical Society.

features with its lighter cousin lithium, in certain respects sodium behaves quite differently. For instance, although all alkalis share the bcc and fcc low pressure structures, sodium adopts distinct (and quite novel) structures at high pressures. Furthermore, sodium is predicted to have a vanishingly small superconducting transition temperature in the bcc phase, and to have $T_c < 1$ K in the fcc phase [68,69], in stark contrast to the $T_c \simeq 20$ K found in lithium.

The most important difference between sodium and lithium is the presence of *p* states in the core of Na. It is instructive to investigate the consequences of this difference for the band structure, as was done by Neaton and Ashcroft [74]. They computed the bands of both elements in the fcc structure at large compressions (in fact at compressions beyond the range of stability of fcc in both systems). As can be seen in Figure 9, the valence band of lithium is no longer free electron-like, exhibiting necks around the L points. Since the core of lithium does not have *p* states, it is relatively easy under pressure for *p* states to penetrate the core regions, thus sampling the nuclear potential and reducing their electrostatic energy, and to hybridize with the *s* states. Sodium, on the other hand, already has *p* states in its core; since orbitals with *p* character must be orthogonal to these states, they are effectively pushed out of the core and cannot fully sample the nuclear potential, leading to higher energies. The core of Na does not have *d* states, however, suggesting that under pressure the occupied states will hybridize with *d*

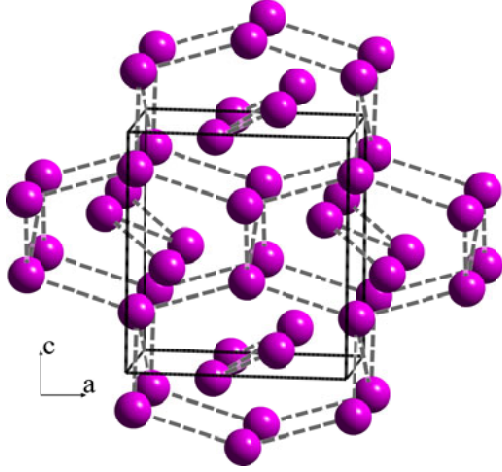


Fig. 10. Crystal structure of Na-*oP8* as viewed down the *b* axis.

orbitals, leading to less symmetric structures in Na than in Li.

3.1 Crystal phases

Sodium, following the same trend as all the alkalis, crystallizes in the bcc structure at ambient conditions and transforms to the fcc phase at 65 GPa. Under further compression, however, it adopts a series of novel and complex lower symmetry structures, and it becomes convenient to label these structures by number, where Na-I corresponds to bcc and Na-II to fcc.

Recent X-ray diffraction studies [75,76] of sodium have revealed that, at a pressure of about 103 GPa, fcc Na transforms to Na-III, a *cI16* phase (space group *I43d*) similar to that adopted by Li [7], which is accompanied by the lowering of the coordination number from 12 to 11.

Na-III is stable up to 117 GPa where it transforms to an orthorhombic structure with space group *Pnma*. This Na-IV phase [75,77], which has also been observed in potassium in the phase K-IV [78] above 54 GPa, contains 8 atoms per unit cell (Pearson symbol *oP8*; see Fig. 10). The *oP8* structure found in the alkali metals is unique among the elements; it belongs to the *MnP* structure type, has been found in many binary compounds [79], but had never before been found in a simple element. At 119 GPa, the lattice parameters for Na-IV are $a = 4.765 \text{ \AA}$, $b = 3.020 \text{ \AA}$, and $c = 5.251 \text{ \AA}$. The 8 atoms in the unit cell are located on two Wyckoff *4c* orbits for $\{x, z\} = \{0.015, 0.18\}$ and $\{0.164, 0.586\}$, respectively. The coordination number further decreases from 11 to 8 or 10 for different atomic sites. The *oP8* structure comprises *ac* planes of atoms with fractional coordinates $y = 1/4$ and $3/4$, but the structure itself is not layered as there are atoms between the layers. The structure can be regarded as consisting of six-sided channels along *b*, and the atomic chains run through the centers of the channels.

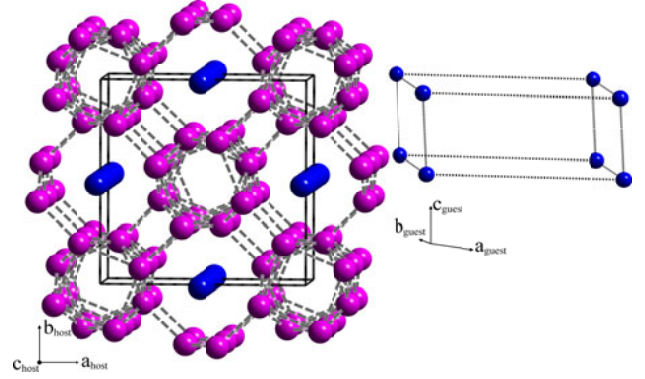


Fig. 11. The structure of Na-tI19 shown in projection down the *c* axis with host atoms in purple and guest atoms in blue.

The existence of Na-V phase above 125 GPa has been established by a recent X-ray diffraction experiment [75,77]. This structure is depicted in Figure 11. Na-V has a surprisingly complex, incommensurate structure which has also been found in Ba-IV [80,81], Sr-V [82], Sc-II [83], Sb-IV [84], As-III [85], Bi-III [85], K-III [86], and Rb-IV [87]. The atomic arrangement is composed of a tetragonal host and an interpenetrating guest structure that is incommensurate with the former along the tetragonal *c* axis. The host structure of Na-V has space group *I4/mcm* which is isostructural with the one observed in K-III and Rb-IV. However, the arrangement of the guest chains is quite different from that of K-III and Rb-IV. The guest arrangement can be understood as a primitive monoclinic structure with space group *P2/m*. At 147 GPa, The refined host lattice parameters are $a_{\text{host}} = 6.995 \text{ \AA}$ and $c_{\text{host}} = 3.399 \text{ \AA}$, with 16 atoms located on the *16k* Wyckoff orbit with $\{x, y\} = \{0.7898, 0.0880\}$; the guest lattice parameters are $a_{\text{guest}} = 4.966 \text{ \AA}$, $b_{\text{guest}} = 4.951 \text{ \AA}$, $c_{\text{guest}} = 2.053 \text{ \AA}$, $\beta = 94.7^\circ$, with an atom located on the *1a* site at $(0, 0, 0)$. Thus, there are $16 + 2c_{\text{host}}/c_{\text{guest}} = 19.3$ in the host unit cell.

Recently, a dense transparent phase of sodium (Na-VI) has been discovered by Ma et al. above 200 GPa [88]. In this phase, the structure of which is sketched in Figure 12, sodium adopts a simple double-hexagonal close-packed (d.h.c.p.) *hP4* structure (space group *P63/mmc*) which is highly compressed along the *c* axis. At 320 GPa, the lattice parameters are $a = 2.874 \text{ \AA}$ and $c = 3.873 \text{ \AA}$ with atoms located on the *2a* $(0, 0, 0)$ and *2d* $(1/3, 2/3, 3/4)$ Wyckoff sites. The *c/a* ratio is 1.391, which is less than half the ideal value of $c/a = 2\sqrt{8/3} = 3.266$ seen in the normal d.h.c.p. structure. The *hP4* structure is less close-packed than *oP8*, with a coordination number of 6. It is noteworthy that in this structure the valence electrons localize at the interstices due to the strong core-valence overlap [88]. As can be found in any d.h.c.p. structure, the stacking of the close-packed layers of Na atoms is CACBCACB... (underlining indicates layers that contain interstitial electron density maxima). However, the interstitial electron density maxima which are located in

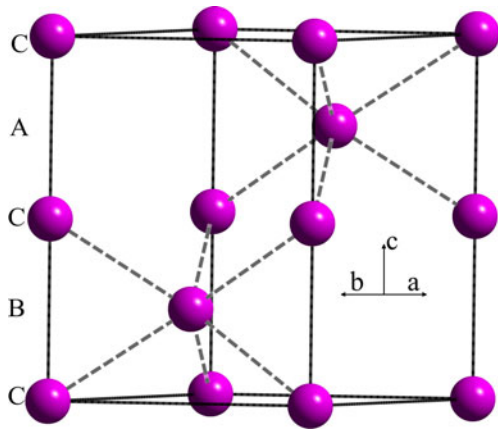


Fig. 12. Crystal structure of Na-*hP4*. “A”, “B”, and “C” represent the different atomic layers.

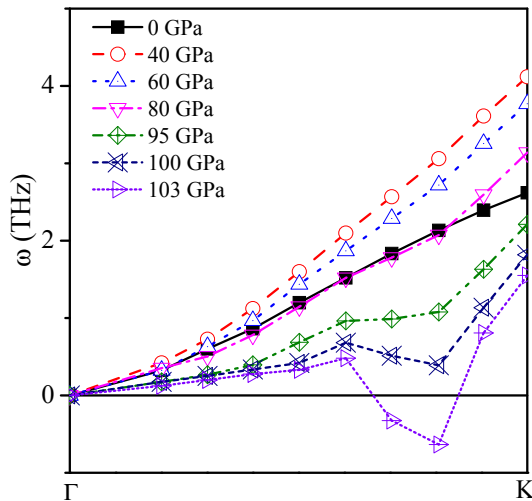


Fig. 13. Calculated TA phonon dispersions of fcc Na along the Γ -K direction for various pressures (frequencies below the zero axis denote imaginary values). The phonons become unstable close to the K symmetry point around 103 GPa for Na. Image reproduced using data from reference [72].

layers A and B form a nearly perfect h.c.p. ABABAB... arrangement [88] (with $c/a \simeq 1.3$ – 1.6 , close to the ideal $c/a = 1.633$ for the h.c.p. structure). This finding suggests that repulsion between the interstitial electron pairs is the major structure-forming interaction in Na-VI. The *hP4* structure can be viewed as analogous to Ni₂In-type structures: the ionic cores form the Ni sublattice and the interstitial density maxima the In sublattice.

3.2 Mechanisms of the high-pressure phase transitions

As was previously mentioned in Section 2.5, phonon softening caused by Fermi surface nesting is believed to be the origin of the $bcc \rightarrow fcc$ phase transition in lithium. As can be seen in Figure 13, a similar TA phonon softening behavior was also predicted in sodium, even though Fermi surface nesting is absent, given that the Fermi sur-

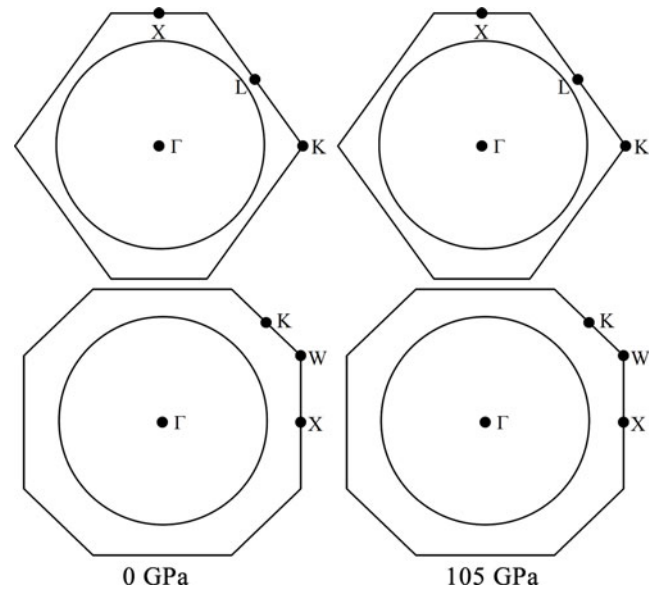


Fig. 14. Fermi surface cross sections of fcc Na at 0 and 105 GPa along (110) (upper panel) and (100) (lower panel) planes. With increasing pressure, there are no noticeable changes in the Fermi surface for both planes. Reprinted figure with permission from [72]. Copyright (2007) by the American Physical Society.

face remains very spherical [72] as can be seen in Figure 14. Although no FSN is predicted for Na, it was shown that pressure increases the strength of the Kohn anomalies in the phonon spectrum [89], explaining the existence of the dynamical instability which eventually induces a phase transition in fcc Na. The certain similarity of the phonon softening and elastic instability between the two light alkali metals indicate a similar sequence of structural transformations, $bcc \rightarrow fcc \rightarrow cI16$.

The crystal phase transitions are also expected from total energy arguments. Degtyareva [44] and Ackland and Macleod [45] found that the reciprocal lattice vector for the first new structural reflections (211) of the *cI16* structure are very close to $2k_F$, thus making these planes almost tangent to the free electron Fermi surface. The first Brillouin zone of *cI16*, limited by 24 such equidistant planes, accommodates the Fermi surface with an electron state filling of 89% (within the NFE model), in agreement with the Hume-Rothery criterion already described in Section 2.3. The lattice distortion brought on by the phase transition to the *cI16* phase leads to an overall electronic energy reduction compared to the parent fcc phase, leading to the stabilization of the new phase under pressure.

Furthermore, it has been shown [46] that the first Brillouin zone of the Na-*oP8* structure consists of 30 Brillouin planes closed to $2k_F$, with a zone filling by electron states of 93%, which is a situation similar to that of the isostructural binary compound AuGa [46]. The volume of the first Brillouin zone in *oP8* is reduced compared to *cI16* due to the new additional Brillouin planes, and once again the Fermi surface – Brillouin zone interaction

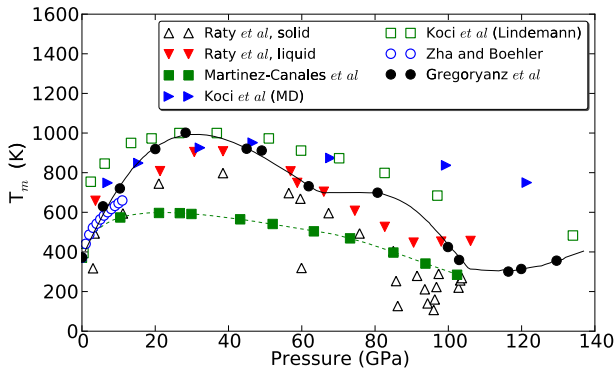


Fig. 15. Sodium experimental melting temperatures as measured by Zha and Boehler [90] and Gregoryanz et al. [91], compared with calculated melting temperatures of Raty et al. [92], Martinez-Canales and Bergara [37] and Koči et al. (molecular dynamics and Lindemann criterion) [93]. All lines are simple guides for the eye.

leads to a reduction of the electronic energy, thus stabilizing the *oP8* structure.

3.3 Melting curve under high pressure

The high-pressure melting of metals has been extensively studied during the last decade because its understanding is important to the fields of shock physics, geophysics, astrophysics, and nuclear materials. The melting property of Na is currently of great theoretical and experimental interest due to its complexity under high pressure.

Recently, Gregoryanz et al. [91] measured the melting curve of Na by high-pressure (HP) high-temperature (HT) X-ray diffraction (XRD) techniques up to 130 GPa (their results are reproduced in Figure 15, along with other experimental results and theoretical calculations). A maximum in the melting curve has been discovered around 31 GPa and 1000 K just above the stability region of the bcc phase, followed by a steep decrease of melting temperature above the fcc phase, reaching a minimum of about 300 K at 118 GPa. Many of the new, complex crystal structures of Na appear in the vicinity of the melting curve minimum. The large pressure range (nearly 90 GPa) of decreasing melting line in Na is quite unique; negative-slope melting lines are usually confined to much smaller pressure ranges, for instance 0.2 GPa in water and 10 GPa in the diamond phase of Si [94]. A liquid-liquid phase transition has been proposed [91] to account for the melting maximum, in analogy with other systems [95,96].

Martinez-Canales and Bergara [37] showed that the presence of the melting curve maximum and the large pressure range over which the melting curve is anomalous could be understood in terms of the Lindemann criterion, which basically relates the melting temperature to the average displacements of the ions in the solid. They noted however that this solid-based criterion was too coarse to properly reproduce the experimental melting curve. Similar calculations were also performed by Koči et al., along with molecular dynamics simulations [93]. Hernández and

Íñiguez [97] have studied the high pressure thermal properties of Na by using first principle molecular dynamics (FPMD). They found that the compressibility of the liquid phase is larger than that of the solid phase and it remains so at high pressures. Hence the liquid phase becomes denser than the solid phase at high pressure, resulting in the change of the slope in the melting line from positive to negative. The high pressure liquid structure has also been characterized by the distribution of bond angles and a rotationally invariant parameter \bar{W}_6 [98]. No evidence was found for a first order liquid-liquid phase transition. It was concluded that, contrary to what was suggested in reference [91], the maximum of the melting line cannot be related to a high pressure liquid-liquid phase transition. Raty et al. [92] performed a more detailed investigation on the structural and electronic properties of compressed sodium, focusing on the second coordination shell. They found that, starting at 30 GPa, the inter-atomic distance in the second shell decreases more rapidly with pressure than that of the first shell in the bcc phase. By comparing the inter-atomic distribution of finite temperature bcc and fcc solids at the same density, with increasing temperature, the first coordination shells of bcc and fcc become almost identical. However, the second coordination shell of the heated fcc is contracted compared to the second coordination shell of the heated bcc, in exactly the same way as it is observed in the liquid between 0 and 60 GPa. Therefore, a transition from bcc to fcc-like local order in the liquid structure has been characterized and is suggested as being responsible for the change of slope in the melting curve. They also pointed out that the structural changes in the liquid to an fcc-like local order cannot explain the anomalous melting above 60 GPa, where the solid below the melting line adopts the fcc structure. As pressure is further increased, the first coordination shell splits and the coordination drops from 13 at 60 GPa to 8 at 105 GPa. The local order of the liquid corresponding to the new coordination is very similar to a distorted bcc structure, *cI16*, which is the stable solid phase of Na above 103 GPa. A pseudogap opens at the Fermi Level in the liquid DOS above 65 GPa, a feature not found in the fcc solid, but is identical to the pseudogap in the high pressure *cI16* crystal. The appearance of this pseudogap at the Fermi level lowers the energy of the valence electrons sufficiently to overcome the cost of increased repulsion associated with local distortions and the loss in entropy compared to the non-distorted liquid. As a result, the melting temperature continues to decrease with pressure. Once the underlying solid goes through the fcc to *cI16* phase transition, the slope of the melting curve becomes positive again since a pseudogap opens in the solid as well. It was found that the *s-p* charge transfer is crucial to understand this symmetry-breaking in molten sodium, which is counterintuitive for a HP and HT liquid.

3.4 Metal to insulator phase transition

Usually, the widths of the valence and conduction bands increase under pressure. As a result, under sufficient

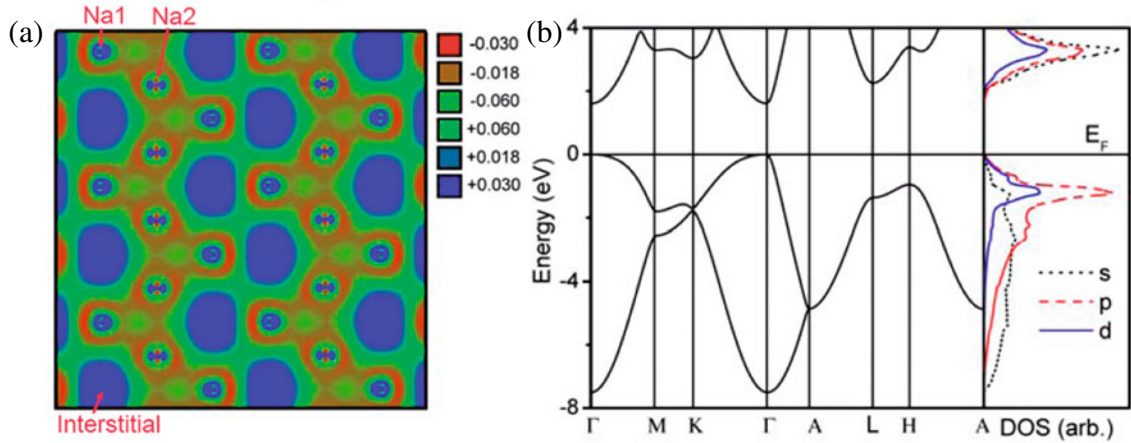


Fig. 16. (a) Difference charge density plotted in the (110) plane at 320 GPa. It is clear that the valence electrons are localized in the interstices. (b) Band structure (left panel) and partial densities of states (right panel) of Na-*hP4* at 300 GPa.

compression, these bands in a semiconductor (insulator) will overlap, leading to the Wilson phase transition to a metallic state. The opposite behavior, namely a metal becoming an insulator under pressure, is more surprising, which is why the initial prediction of Neaton et al. [2,74] that the α -Ga structure, which is insulating and in which the ions are paired, should be stable at high pressure attracted a lot of attention. Although sodium was found to be a poor metal in the Na-IV and Na-V structures by optical measurements [99], the insulating α -Ga structure proposed by Neaton and Ashcroft [2,74] was never observed experimentally. In order to find other candidate high pressure atomic arrangements, Ma et al. [88] performed structure searches for Na by using an *ab initio* evolutionary algorithm [21,22,34,88,100,101] over a wide pressure range. The simulations revealed a simple but squeezed *hP4* structure above 260 GPa. The electronic structure of Na-*hP4* (Fig. 16b) gives rise to an intriguing insulating state characterized by a large occupancy of *d* orbitals that are involved in *p-d* hybridizations. GW calculation gave a large band gap of 3.2 eV at 300 GPa. HP-XRD and Raman spectra experiments confirmed that the predicted *hP4* structure is stable above 200 GPa. It is also found that sodium becomes optically transparent around 200 GPa which directly demonstrates the insulating nature of the *hP4* phase. It was suggested that the increasing *p-d* hybridization upon compression plays a very important role in the emergence of the insulating electronic state, driving electron localization (Fig. 16a). Moreover, transparent sodium behaves as an unconventional inorganic electride [102], where the interstitial electron density maxima play the role of anions. It is noteworthy that the theoretical transition pressure is slightly higher than the experiment results. This is because measurements were performed at room temperature; zero-temperature calculations neglected entropy contributions and lattice dynamics which may stabilize the structure at a lower pressure. Furthermore, Gatti et al. [103] have calculated the absorption and electron-energy loss spectroscopy (EELS) spectra to confirm the crystal structure of transparent

dense sodium. They discovered an unusual kind of charge-transfer exciton that proceeds from the interstitial distribution of valence electrons which supported the results of Ma et al. [88]. They also found that the spectra are quite anisotropic, which is essentially linked to the symmetry of the crystal structure. In the *hP4* phase, sodium becomes transparent at a lower pressure in one polarization direction while still being “metallic” in another. A measurement of the spectra for two distinct polarizations could be used to further confirm that transparent sodium crystallizes in the *hP4* structure.

4 Conclusion

The light alkalis lithium and sodium have received a lot of attention in recent years thanks to improved experimental techniques and new insights provided by theoretical calculations. Under high pressure, these elements, which at ambient conditions crystallize in highly symmetric close-packed structures and can be described by the NFE model, go through phase transitions into complex low-symmetry structures, many of which have been observed for the first time. Most of the complex structures have been solved, but some of them are still not fully resolved, e.g. *oC88*. As Li is quite light, quantum effects associated with its lattice dynamics could be important to determine the actual high pressure phases. Theoretical studies at finite temperature together with high precision XRD experiments will be required to resolve the mysterious high pressure structures in Li.

Several models have been proposed to explain the pressure induced structural transformations in these light alkalis. Although the mechanism of the lower pressure bcc to fcc phase transition is well established, the higher pressure complex phase transitions are not as fully understood. Simple models such as charge transfer and the Hume-Rothery mechanism can give a qualitative explanation but cannot guarantee sufficient accuracy to allow the determination of structural sequences. Understanding

the structural behavior of the light alkalis at high pressure remains a challenge.

At ambient conditions, lithium and sodium behave in similar ways because they are well described by a picture where the core electrons are tightly bound to the nuclei and the valence electrons are nearly free. Pressure progressively destroys this simple picture; correspondingly, the properties of lithium and sodium need not be analogous under pressure. For instance, the structures adopted by these elements are quite different beyond their common bcc \rightarrow fcc transition. Furthermore, lithium becomes a good superconductor, reaching a maximum T_c of about 14 K at 30 GPa, whereas sodium remains non superconducting.

Despite their differences, lithium and sodium also show similarities which can be understood in terms of a new emerging paradigm, interstitial electronic localization. Indeed, although the high pressure structures are different, they tend to be non-close packed, allotting space for the electrons to pile up in. Furthermore, both systems undergo a metal-to-(band) insulator transition, which can be viewed as driven by this localization.

Much has been learned about the effect of pressure on the alkalis, but much remains to be done. Many pressing challenges present themselves: for instance, the local order in the lithium melt in the anomalous region remains to be measured; does it in fact behave as simulation suggests? Can the anomalous isotope coefficient in the $oC40$ phase be explained? Technical difficulties must be resolved before samples can be pressurized beyond what is currently achievable, but the light alkalis are sure to keep surprising and challenging us as we move towards higher and higher compression.

Y.X. and Y.M. thank the National Natural Science Foundation of China for financial support under grant numbers 10874054, 91022029 and 11025418. B.R. and A.B. acknowledge financial support from UPV/EHU (Grant No. IT-366-07) and the Spanish Ministry of Science and Innovation (Grant No. FIS2010-19609-C02-00).

References

1. N.W. Ashcroft, D. Mermin, *Solid State Physics* (Thompson Learning, Inc., 1976)
2. J.B. Neaton, N.W. Ashcroft, *Nature* **400**, 141 (1999)
3. R.M. Martins, *Nature* **400**, 117 (1999)
4. A. Bergara, J.B. Neaton, N.W. Ashcroft, *Phys. Rev. B* **62**, 8494 (2000)
5. J.C. Boettger, S.B. Trickey, *Phys. Rev. B* **32**, 3391 (1985)
6. B. Rousseau, N.W. Ashcroft, *Phys. Rev. Lett.* **101**, 046407 (2008)
7. M. Hanfland, K. Syassen, N.E. Christensen, D.L. Novikov, *Nature* **408**, 174 (2000)
8. M.I. McMahon, R.J. Nelmes, *Chem. Soc. Rev.* **35**, 943 (2006)
9. M. Hanfland, I. Loa, K. Syassen, U. Schwarz, K. Takemura, *Solid State Commun.* **112**, 123 (1999)
10. A.W. Overhauser, *Phys. Rev. Lett.* **53**, 64 (1984)
11. W. Schwarz, O. Blaschko, *Phys. Rev. Lett.* **65**, 3144 (1990)
12. A.Y. Liu, A.A. Quong, J.K. Freericks, E.J. Nicol, E.C. Jones, *Phys. Rev. B* **59**, 4028 (1999)
13. T. Matsuoka, S. Onoda, M. Kaneshige, Y. Nakamoto, K. Shimizu, T. Kagayama, Y. Ohishi, *J. Phys. Conf. Ser.* **121**, 052003 (2008)
14. T. Matsuoka, K. Shimizu, *Nature* **458**, 186 (2009)
15. V.V. Struzhkin, M.I. Eremets, W. Gan, H.K. Mao, R.J. Hemley, *Science* **298**, 1213 (2002)
16. A.F. Goncharov, V.V. Struzhkin, H.K. Mao, R.J. Hemley, *Phys. Rev. B* **71**, 184114 (2005)
17. J.S. Tse, D.D. Klug, T. Iitaka, *Phys. Rev. B* **73**, 212301 (2006)
18. C.L. Guillaume, E. Gregoryanz, O. Degtyareva, M.I. McMahon, M. Hanfland, S. Evans, M. Guthrie, S.V. Sinogeikin, H.K. Mao, *Nature Phys.* **7**, 211 (2011)
19. R. Rousseau, K. Uehara, D. Klug, J.S. Tse, *Chem. Phys. Chem.* **6**, 1703 (2005)
20. A.R. Oganov, C.W. Glass, S. Ono, *Earth Plan. Sci. Lett.* **241**, 95 (2006)
21. A.R. Oganov, C.W. Glass, *J. Chem. Phys.* **124**, 244704 (2006)
22. C.W. Glass, A.R. Oganov, N. Hansen, *Comput. Phys. Commun.* **175**, 713 (2006)
23. C.J. Pickard, R.J. Needs, *Phys. Rev. Lett.* **97**, 045504 (2006)
24. C.J. Pickard, R.J. Needs, *Nature Phys.* **3**, 473 (2007)
25. C.J. Pickard, R.J. Needs, *Phys. Rev. B* **76**, 144114 (2007)
26. C.J. Pickard, R.J. Needs, *Nature Mater.* **7**, 775 (2008)
27. Y. Wang, J. Lv, L. Zhu, Y. Ma, *Phys. Rev. B* **82**, 094116 (2010)
28. P. Li, G. Gao, Y. Wang, Y. Ma, *J. Phys. Chem. C* **114**, 21745 (2010)
29. More information about the CALYPSO code, by Y. Ma, Y. Wang, J. Lv, L. Zhu, can be found at <http://nlshmlab.jlu.edu.cn/~calypso.html>
30. M. Marqués, M.I. McMahon, E. Gregoryanz, M. Hanfland, C.L. Guillaume, C.J. Pickard, G.J. Ackland, R.J. Nelmes, *Phys. Rev. Lett.* **106**, 095502 (2011)
31. Y. Yao, J.S. Tse, D.D. Klug, *Phys. Rev. Lett.* **102**, 115503 (2009)
32. J. Lv, Y. Wang, L. Zhu, Y. Ma, *Phys. Rev. Lett.* **106**, 015503 (2011)
33. C.J. Pickard, R.J. Needs, *Phys. Rev. Lett.* **102**, 146401 (2009)
34. Y. Ma, A.R. Oganov, Y. Xie, *Phys. Rev. B* **78**, 014102 (2008)
35. I. Tamblyn, J.Y. Raty, S.A. Bonev, *Phys. Rev. Lett.* **101**, 075703 (2008)
36. A. Lazicki, Y. Fei, R.J. Hemley, *Solid State Commun.* **150**, 625 (2010)
37. M. Martinez-Canales, A. Bergara, *J. Phys. Chem. Solids* **69**, 2151 (2008)
38. R. Boehler, *Phys. Rev. B* **27**, 6754 (1983)
39. H. Luedemann, G.C. Kennedy, *J. Geophys. Res.* **73**, 2795 (1968)
40. E.R. Hernandez, A. Rodriguez-Prieto, A. Bergara, D. Alfè, *Phys. Rev. Lett.* **104**, 185701 (2010)
41. P. Hohenberg, W. Kohn, *Phys. Rev.* **136**, B864 (1964)
42. W. Kohn, L.J. Sham, *Phys. Rev.* **140**, A1133 (1965)

43. A. Rodriguez-Prieto, A. Bergara, V.M. Silkin, P.M. Echenique, *Phys. Rev. B* **74**, 172104 (2006)
44. V.F. Degtyareva, *High Press. Res.* **23**, 253 (2003)
45. G.J. Ackland, I.R. Macleod, *New J. Phys.* **6**, 138 (2004)
46. V.F. Degtyareva, O. Degtyareva, *New J. Phys.* **11**, 063037 (2009)
47. A. Bergara, J.B. Neaton, N.W. Ashcroft, *Int. J. Quantum Chem.* **91**, 239 (2003)
48. A. Rodriguez-Prieto, A. Bergara, *Phys. Rev. B* **72**, 125406 (2005)
49. V.M. Silkin, A. Rodriguez-Prieto, A. Bergara, E.V. Chulkov, P.M. Echenique, *Phys. Rev. B* **75**, 172102 (2007)
50. A. Rodriguez-Prieto, V.M. Silkin, A. Bergara, P. Echenique, *New J. Phys.* **10**, 053035 (2008)
51. I. Errea, A. Rodriguez-Prieto, B. Rousseau, V.M. Silkin, A. Bergara, *Phys. Rev. B* **81**, 205105 (2010)
52. R.E. Alonso, S. Sharma, C. Ambrosch-Draxl, C.O. Rodriguez, N.E. Christensen, *Phys. Rev. B* **73**, 064101 (2006)
53. Y. Xie, Y.M. Ma, T. Cui, Y. Li, J. Qiu, G.T. Zou, *New J. Phys.* **10**, 063022 (2008)
54. E.C. Bain, *Trans. AIME* **70**, 25 (1924)
55. V.F. Degtyareva, *Phys.-Uspekhi* **49**, 369 (2006)
56. B.T. Matthias, *Phys. Rev.* **97**, 74 (1955)
57. N.W. Ashcroft, *Nature* **419**, 569 (2002)
58. A.Y. Liu, M.L. Cohen, *Phys. Rev. B* **44**, 9678 (1991)
59. C.F. Richardson, N.W. Ashcroft, *Phys. Rev. B* **55**, 15130 (1997)
60. J. Tuoriniemi, K. Juntunen-Nurmilaukas, J. Uusvuori, E. Pentti, A. Salmela, A. Sebedash, *Nature* **447**, 187 (2007)
61. T.H. Lin, K.J. Dunn, *Phys. Rev. B* **33**, 807 (1986)
62. K. Shimizu, H. Ishikawa, D. Takao, T. Yagi, K. Amaya, *Nature* **419**, 597 (2002)
63. J.S. Schilling, *High Press. Res.* **26**, 145 (2006)
64. S. Deemyad, J.S. Schilling, *Phys. Rev. Lett.* **91**, 167001 (2003)
65. J.S. Schilling, in *Handbook of High Temperature Superconductivity: Theory and Experiment*, edited by J. Schrieffer, J. Brooks (Springer Verlag, 2007)
66. Y. Yao, J.S. Tse, K. Tanaka, F. Marsiglio, Y. Ma, *Phys. Rev. B* **79**, 054524 (2009)
67. N.E. Christensen, D.L. Novikov, *Phys. Rev. Lett.* **86**, 1861 (2001)
68. N.E. Christensen, D.L. Novikov, *Phys. Rev. B* **73**, 224508 (2006)
69. L. Shi, D.A. Papaconstantopoulos, *Phys. Rev. B* **73**, 184516 (2006)
70. M. Luders, M.A.L. Marques, N.N. Lathiotakis, A. Floris, G. Profeta, L. Fast, A. Continenza, S. Massidda, E.K.U. Gross, *Phys. Rev. B* **72**, 024545 (2005)
71. G. Profeta, C. Franchini, N.N. Lathiotakis, A. Floris, A. Sanna, M.A.L. Marques, M. Luders, S. Massidda, E.K.U. Gross, A. Continenza, *Phys. Rev. Lett.* **96**, 047003 (2006)
72. Y. Xie, J.S. Tse, T. Cui, A.R. Oganov, Z. He, Y. Ma, G. Zou, *Phys. Rev. B* **75**, 064102 (2007)
73. D. Kasinathan, J. Kuneš, A. Lazicki, H. Rosner, C.S. Yoo, R.T. Scalettar, W.E. Pickett, *Phys. Rev. Lett.* **96**, 047004 (2006)
74. J.B. Neaton, N.W. Ashcroft, *Phys. Rev. Lett.* **86**, 2830 (2001)
75. E. Gregoryanz, L.F. Lundegaard, M.I. McMahon, C. Guillaume, R.J. Nelmes, M. Mezouar, *Science* **320**, 1054 (2008)
76. M.I. McMahon, E. Gregoryanz, L.F. Lundegaard, I. Loa, C. Guillaume, R.J. Nelmes, A.K. Kleppe, M. Amboage, H. Wilhelm, A.P. Jephcoat, *Proc. Natl. Acad. Sci. USA* **104**, 17297 (2007)
77. L.F. Lundegaard, E. Gregoryanz, M.I. McMahon, C. Guillaume, I. Loa, R.J. Nelmes, *Phys. Rev. B* **79**, 064105 (2009)
78. L.F. Lundegaard, M. Marqués, G. Stinton, G.J. Ackland, R.J. Nelmes, M.I. McMahon, *Phys. Rev. B* **80**, 20101 (2009)
79. W.B. Pearson, *The Crystal Chemistry Physics of Metals Alloys* (Wiley, New York, 1972)
80. R.J. Nelmes, D.R. Allan, M.I. McMahon, S.A. Belmonte, *Phys. Rev. Lett.* **83**, 4081 (1999)
81. M. McMahon, R. Nelmes, *Z. Kristallogr* **219**, 742 (2004)
82. M.I. McMahon, T. Bovornratanaraks, D.R. Allan, S.A. Belmonte, R.J. Nelmes, *Phys. Rev. B* **61**, 3135 (2000)
83. M.I. McMahon, L.F. Lundegaard, C. Hejny, S. Falconi, R.J. Nelmes, *Phys. Rev. B* **73**, 134102 (2006)
84. O. Degtyareva, M.I. McMahon, R.J. Nelmes, *Phys. Rev. B* **70**, 184119 (2004)
85. M.I. McMahon, O. Degtyareva, R.J. Nelmes, *Phys. Rev. Lett.* **85**, 4896 (2000)
86. M.I. McMahon, R.J. Nelmes, U. Schwarz, K. Syassen, *Phys. Rev. B* **74**, 140102 (2006)
87. M.I. McMahon, S. Rekhi, R.J. Nelmes, *Phys. Rev. Lett.* **87**, 055501 (2001)
88. Y. Ma, M. Eremets, A.R. Oganov, Y. Xie, I. Trojan, S. Medvedev, A.O. Lyakhov, M. Valle, V. Prakapenka, *Nature* **458**, 182 (2009)
89. B. Rousseau, I. Errea, A. Bergara, *J. Phys. Chem. Solids* **71**, 1159 (2010)
90. C.S. Zha, R. Boehler, *Phys. Rev. B* **31**, 3199 (1985)
91. E. Gregoryanz, O. Degtyareva, M. Somayazulu, R.J. Hemley, H.K. Mao, *Phys. Rev. Lett.* **94**, 185502 (2005)
92. J.Y. Raty, E. Schwegler, S.A. Bonev, *Nature* **449**, 448 (2007)
93. L. Koči, R. Ahuja, L. Vitos, U. Pinsook, *Phys. Rev. B* **77**, 132101 (2008)
94. M. Kaczmariski, O.N. Bedoya-Martínez, E.R. Hernández, *Phys. Rev. Lett.* **94**, 095701 (2005)
95. Y. Katayama, T. Mizutani, W. Utsumi, O. Shimomura, M. Yamakata, K.I. Funakoshi, *Nature* **403**, 170 (2000)
96. G. Monaco, S. Falconi, W.A. Crichton, M. Mezouar, *Phys. Rev. Lett.* **90**, 255701 (2003)
97. E.R. Hernández, J. Íñiguez, *Phys. Rev. Lett.* **98**, 055501 (2007)
98. P.J. Steinhardt, D.R. Nelson, M. Ronchetti, *Phys. Rev. B* **28**, 784 (1983)
99. A. Lazicki, A.F. Goncharov, V.V. Struzhkin, R.E. Cohen, Z. Liu, E. Gregoryanz, C. Guillaume, H.K. Mao, R.J. Hemley, *Proc. Nat. Acad. Sci.* **106**, 6525 (2009)
100. A.R. Oganov, J. Chen, C. Gatti, Y. Ma, Y. Ma, C.W. Glass, Z. Liu, T. Yu, O.O. Kurakevych, V.L. Solozhenko, *Nature* **457**, 863 (2009)
101. Y. Ma, A. Oganov, Z. Li, Y. Xie, J. Kotakoski, *Phys. Rev. Lett.* **102**, 65501 (2009)
102. J. Dye, *Science* **247**, 663 (1990)
103. M. Gatti, I.V. Tokatly, A. Rubio, *Phys. Rev. Lett.* **104**, 216404 (2010)